Ceramics

Defect structures of sodium and chloride co-substituted hydroxyapatite and its osseointegration capacity

Dong Su Yoo[1], Jung Sang Cho[2], Yong-Chae Chung[1], and Sang-Hoon Rhee[2,3,*]

[1] Department of Materials Science and Engineering, Hanyang University, Seoul 04763, South Korea

[2] Interdisciplinary Program of Bioengineering, College of Engineering, Seoul National University, Seoul 08826, South Korea

[3] Department of Dental Biomaterials Science, Dental Research Institute, School of Dentistry, Seoul National University, Daehak-ro 101, Jongno-gu, Seoul 03080, South Korea

ABSTRACT

A defect structure and osseointegration capacity of sodium and chloride co-substituted hydroxyapatite (NaClAp) were newly studied. The NaClAp was prepared by reacting H_3PO_4 and $Ca(OH)_2$ with $NaNO_3$ and NH_4Cl followed by sintering; pure hydroxyapatite (HAp) was synthesized as a control. After sintering, the co-substitution of Ca and OH with Na and Cl, respectively, produced charged point defects at Ca and PO_4 sites. Also, OH molecules partially adopted a head-on structure. The calculated total system energy of NaClAp was higher, whereas the binding energies between each constituent elements and system were lower than those of HAp. These results suggest that NaClAp was less stable than HAp, due to the formation of various defects by co-substitution of Na and Cl. Indeed, NaClAp exhibited higher dissolution behavior in simulated body fluid (SBF) compared with HAp. Accordingly, this increased the capability to produce low crystalline hydroxyl carbonate apatite, likely due to the increasing degree of apatite supersaturation in SBF. Besides, the NaClAp granules showed noticeable improvements in osseointegration capacity four weeks after in vivo test compared with HAp. Collectively, these results imply that the defects made by multiple ion substitutions are useful to increase osseointegration capacity of hydroxyapatite.

Introduction

An alternative to bone apatite for bone grafts, synthetic hydroxyapatite prepared at high temperature has been considered. Despite its similarities, the synthetic hydroxyapatite prepared at high temperature differs from bone apatite in that it has a higher crystallinity, larger grains, and an exact stoichiometry, which yield low surface reactivity in vivo [1]. Indeed, dense hydroxyapatite with large grains shows lower osseointegration capacity relative to that with small grains [2], and this harmfully increases patient recovery period. Thus, diverse techniques have been proposed to enhance osseointegration capacity of the artificial hydroxyapatite such as altering the sintering time [2], temperature [3], granule size [4, 5], electrical polarity [6], porosity [7], and substituting foreign ions [8–19].

Many attempts have been made to explain the defect structures of the hydroxyapatite substituted with cationic ions having different electronic valences. Several studies tried to show the entire defect structures and the process of defect formation [8, 10, 19]. However, the suggested defect structures were incomplete because they did not exactly follow three rules for analyzing defect chemical reactions such as site, charge, and mass balances [8, 10, 19]. The Kröger–Vink notation [20] coupled with three rules for analyzing defect chemical reactions is necessary to solve this problem.

The substitution of single foreign element, which had different electronic valences, electronegativity, and sizes, with one of the constituent elements of hydroxyapatite increased the total system energy and decreased the binding energies between constituent elements of apatite and the system [19, 21]. The different valences, electronegativity, and sizes of foreign elements are expected to make the hydroxyapatite unstable energetically after sintering by causing lattice distortions and point defects. This will cause the dissolution of constituent elements in vivo and consequently enhance the osseointegration capacity by the formation of low crystalline hydroxyl carbonate apatite (HCA).

Herein, we attempted to maximize the total system energy by simultaneously replacing two constituent elements of hydroxyapatite, Ca and OH, with Na and Cl, respectively. There have been no studies about the co-substitution of different elements with different charges. We describe in detail the synthesis of Na and Cl co-substituted hydroxyapatite (NaClAp) and the formation mechanism of defect structures during the process using Kröger–Vink notation [20]. The NaClAp was then evaluated, relative to pure HAp, in regard to HCA producing capability in simulated body fluid (SBF) and osseointegration capacity. The ab initio method was used to analyze the improved osseointegration capacity of NaClAp compared to HAp.

Materials and methods

Syntheses of Na and Cl co-substituted hydroxyapatite and pure hydroxyapatite

The $Ca(OH)_2$, H_3PO_4, $NaNO_3$, and NH_4Cl were used to produce Na and Cl co-substituted hydroxyapatite. The molar ratio of $Ca(OH)_2/H_3PO_4/NaNO_3/NH_4Cl$ was 9.7:6:0.3:1.0.

The $Ca(OH)_2$ powder was produced by calcining $CaCO_3$ (Wako Pure Chemicals) at 1050 °C for 3 h, and then slaking the resultant CaO with water. In order to synthesize Na and Cl co-substituted hydroxyapatite, the $NaNO_3$ (Aldrich) and NH_4Cl (Aldrich) were dissolved in a 1 M $Ca(OH)_2$ suspension. Next, 1 M H_3PO_4 (Wako Pure Chemicals) was reacted with the $Ca(OH)_2$ mixture at room temperature with fast stirring. This process was repeated only apatite was identified after sintering the precipitate at 1100 °C for 1 h. The suspension was matured for 1 d at ambient condition and subsequently dried completely in a forced air circulation oven at 70 °C to retain water-soluble $NaNO_3$ and NH_4Cl. The dried block was subsequently crushed and sieved to separate powders under 75 μm. From now, the apatite substituted by Na and Cl together is abbreviated as NaClAp. Single hydroxyapatite powder was made as a control conforming to the identical processes except for adding $NaNO_3$ and NH_4Cl. After this, single hydroxyapatite is abbreviated as HAp.

The HAp and NaClAp disks ($\phi 10 \times t2$ mm) were made under a 30 MPa to evaluate their capabilities of producing HCA and dissolution in the SBF. After being embedded the disks into the pre-sintered and ground NaClAp granules to suppress the volatilization of Na and Cl from the sample, the sintering was conducted at 1100 °C for 3 h at a ramping rate of 5 °C/min.

For osseointegration capacity tests, porous apatite granules were prepared using previously reported method [19]. In brief, polyethylene glycol (PEG; Mw 10000, Aldrich) powder was used as a porogen by generating two different size distributions (75–212 and 212–425 μm) by sieving. The two sizes of PEG were mechanically mixed with the apatite powder. The mixing ratio among apatite, small-sized PEG (75–212 μm), and large-sized PEG (212–425 μm) was 60: 20: 20 (wt %). The resulting mixtures were compacted into disks with a diameter of 50 mm and a height of 30 mm under a pressure of 20 MPa, followed by sintering at 1100 °C for 3 h at a heating rate of 5 °C/min. The sintered disks were fractured and sieved to generate granules with a size range of 425–600 μm.

Evaluation of HCA producing capability in SBF

The HCA producing capability of HAp and NaClAp was evaluated in SBF [22]. The SBF was made by dissolving $CaCl_2$, $MgCl_2 \cdot 6H_2O$, KCl, NaCl, $NaHCO_3$, Na_2SO_4, and $K_2HPO_4 \cdot 3H_2O$ in deionized water. The tris(hydroxymethyl) aminomethane and 1 M HCl solution were used to buffer the SBF at pH 7.25. It was subsequently filtered (0.22 μm, Millipore). Before the test, a UV lamp was used for 30 min to sterilize the samples. Subsequently, they were immersed into 30 ml of SBF and then kept for different time intervals at 36.5 °C. Next, the samples were mildly rinsed three times with deionized water to prevent the precipitation of various salts after drying and then air-dried under ambient conditions.

Analysis

A field emission scanning electron microscopy (FE-SEM; S-4700, Hitachi) and X-ray diffractometer (XRD; D8 Advance, Bruker) were used to evaluate the microstructures and crystal phases, respectively. Microstructural characteristics were determined with image analysis software (ImageJ, NIH). The shortest diagonal of each grain was determined, and it was used to represent the grain size. The average grain size was determined by measuring at least 500 crystals. Relative densities of the sintered samples were measured by Archimedes' principle. The lattice constants of the sintered HAp and NaClAp were assessed with Rietveld refinement (TOPAS v.2.0, Bruker)

[23]. The least squares approach was repeated to refine a theoretical line profile until it matches the measured profile.

An electron probe X-ray microanalyzer (EPMA; JXA-8500F, JEOL) was used to characterize the existence of Ca, P, Na, and Cl on the apatites. The 102×102 μm area was examined with a resolution of 0.4 μm.

The Fourier-transform infrared spectroscopy (FT-IR; Spectrum 100, PerkinElmer) was used to assess the functional groups of the samples at a resolution of 4 cm^{-1}. The sintered samples were ground and then mixed 350-fold with potassium bromide after drying for 1 d in a convection oven at 70 °C. The potassium bromide pellets with the samples were compacted into disks under a compression of 1 MPa. The background noise was corrected using the pure potassium bromide disk.

The chemical composition of sintered NaClAp was determined by an inductively coupled plasma atomic emission spectroscopy (ICP-AES; Optima-8300, PerkinElmer) and ion chromatography (IC; ICS-2000, Dionex) after dissolving it in 1 N HCl solution. The concentrations of Ca, P, Na, and Cl dissolved from the samples into SBF after various soaking times were also measured by ICP-AES and IC. For measuring the pH of the SBF, a pH meter (DK-20, Horiba) was used. For each soaking time, five samples were used and the values were averaged and showed as the mean ± standard deviation.

First principle calculation of total system energy

The first principle calculations were performed to optimize structures of the apatites. The density functional theory was used with the exchange–correlation energy functional treated by Perdew–Burke–Ernzerhof (PBE) from a generalized gradient approximation [24] with a projector augmented wave [25]. In the hydroxyapatite unit cell, 5% of Ca and 25% of OH were replaced by Na and Cl, respectively, to optimize ab initio calculation procedure. The self-consistent electronic density function and total energy were calculated with a plane-wave basis set that had a cutoff energy of 400.0 eV (29.40 Ry) using the Vienna ab initio simulation package [26]. The self-consistent field calculation was repeated until the total energy difference of the systems between the adjacent iterating steps was less than 10^{-6} eV. All

constituent elements in the apatite system were fully relaxed for structural optimization until the maximum Hellmann–Feynman forces [27] reached a range of ± 2.0 meV/Å with an ionic relaxation scheme based on the conjugate gradient method [28]. The non-shifted and Γ-point centered $3 \times 3 \times 3$ and $3 \times 3 \times 1$ k-point grids with the Monkhorst–Pack scheme were used to sample Brillouin zone [29]. For Brillouin zone integration, a linear tetrahedron method with Blöchl correction was implemented for the smearing method [30].

Osseointegration capacity

Animal experiment

For analyzing the osseointegration capacity of HAp and NaClAp, eight New Zealand white male rabbits weighing 2–2.5 kg were used. The surgery was carried out under both general (ketamine; 7.5 mg/kg, Yuhan and Rompun; 3.5 mg/kg, Bayer Korea) and local (2% lidocaine with 1:100000 epinephrine) anesthesia. Iodine and 5% chlorhexidine digluconate were used to disinfect the surgical site. A midline opening was conducted from the nasofrontal area to the external occipital protuberance. Then, a skin periosteal flap was raised to expose the calvarial bone surface. A trephine bur (8 mm in diameter, 3i-Implant Innovations) was then used to outline the boundary of the bone defect. Subsequently, the bicortical calvarial bone was detached with a round bur. Copious saline irrigation was used during the processes. Two defects were made for each rabbit. Afterward, the respective defects were filled with one of each of the two samples. Next, the closing of periosteum and skin in layers was conducted with 4–0 chromic gut sutures (Ethicon). After three days of surgery, antibiotics were injected intramuscularly.

Four weeks after implantation, all eight rabbits were sacrificed. The 10% neutral buffered formalin was used to fix the bone collected en bloc. A super low-viscosity embedding media (Technovit 7200, Exakt Apparatebau) was used after washing with water and dehydrating to fix the samples without decalcification. Coronally section of the samples was made at a thickness of 80 μm using a diamond disk saw (Secotom-15, Struers). Then, grinding and polishing to 40 μm were carried out using a polisher (Tegrapol-35, Struers). The staining was conducted with Sanderson's Rapid Bone Stain™ and a van

Gieson counterstain (Surgipath Medical Industries). The histology was observed using an optical microscope (DM5000B, Leica). Areal percentages of new bone, grafted samples, and connective tissues from whole defect area were measured with image analysis software (ImageJ, NIH).

Animal research ethics

Approval was obtained for all animal experiments, which were performed according to the guidelines of the Institutional Animal Care and Use Committee of Seoul National University (SNU-120222-1).

Statistical analysis

The SPSS® Statistics (Ver. 25, SPSS, IBM®) was used for statistical analyses. Data were examined with a paired Student's t test and represented as the mean $\pm$ standard deviation with significant level of $P < 0.01$.

Results

The phase analyses were carried out to confirm the formations of HAp and NaClAp using XRD (Fig. 1). As a result, only an apatite phase with low crystallinity was identified for both specimens. The functional groups of the HAp and NaClAp powders were evaluated by FT-IR (Fig. 2). The band found at
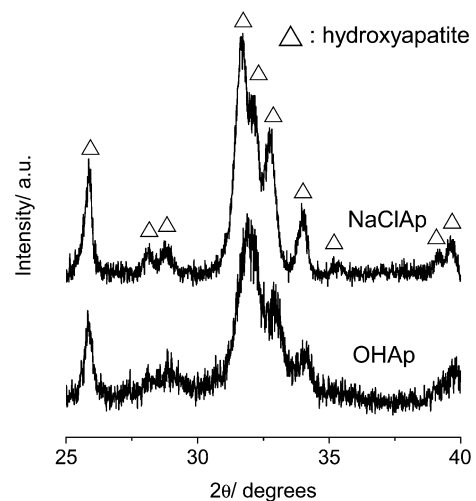

Figure 1 XRD patterns of as-synthesized hydroxyapatite (HAp) and sodium and chloride co-substituted hydroxyapatite (NaClAp) powders. Δ: hydroxyapatite.

875 cm^{-1} was indexed to a bending mode (υ_2) of carbonate [31, 32], while the bands at 1453 and 1421 cm^{-1} were indexed to the bending (υ_3) and stretching (υ_1) modes of carbonate [33], respectively. The band found at about 1383 cm^{-1} was indexed to symmetric stretching mode (υ_3) of nitrate [34], which came from initial NaNO$_3$. All bands except carbonate and nitrate bands were from hydroxyapatite.

The microstructures of the HAp and NaClAp after sintering were observed by FE-SEM (Fig. 3). The grain shapes and sizes were similar for both materials. Specifically, the average grain sizes of HAp and NaClAp were 0.32 ± 0.14 and 0.39 ± 0.16 μm, respectively. The sintered density of HAp was about 98%, while that of NaClAp was about 96%.

The crystal phase analysis was carried out for HAp and NaClAp disks (Fig. 4) with XRD after sintering. The crystal phase of HAp was pure hydroxyapatite (JCPDS 09-0432), whereas that of NaClAp was chlorine-bearing hydroxyapatite (JCPDS 70–0794). In fact, the empirical formula of sintered NaClAp determined by ICP-AES and IC was $Ca_{9.70}Na_{0.10}(PO_4)_{5.32}O_{0.68}(OH)_{1.51}Cl_{0.49}$.

To assess the changes in hydroxyapatite structure due to sintering, the functional groups of HAp and NaClAp were characterized by FT-IR (Fig. 5). In addition to the hydroxyapatite bands, two new sets of bands were determined in the NaClAp. The first set of bands was observed at 3545, 3495, and 3460 cm^{-1} which came from OH–Cl [35]. The second new band was observed at 670 cm^{-1}, which came from –HO:OH– a 'head-on' configuration [36]. All bands
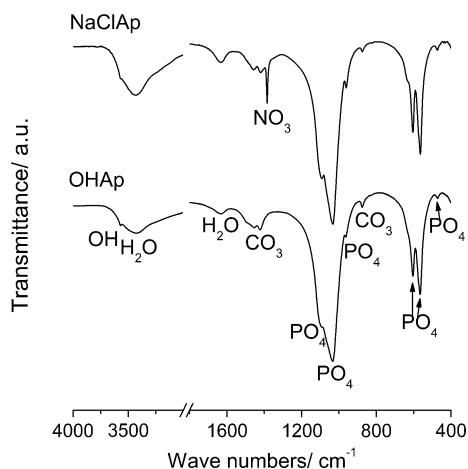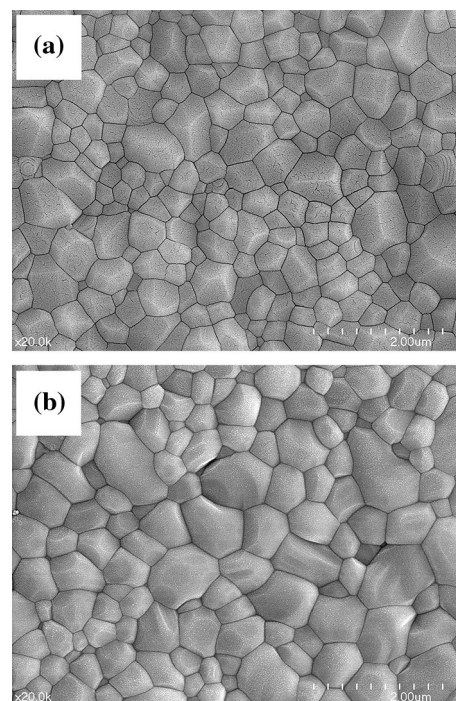

Figure 3 FE-SEM images of **a** hydroxyapatite (HAp) and **b** sodium and chloride co-substituted hydroxyapatite (NaClAp) disks after sintering at 1100 °C for 3 h.

except OH–Cl and –HO:OH– were from hydroxyapatite.

The microstructures of the HAp and NaClAp disks after sintering and corresponding elemental distributions of Ca, P, Na, and Cl measured by EPMA are illustrated in Fig. 6. Only Ca and P were found in the grains of the HAp disk (Fig. 6a). In contrast, Na and Cl, in addition to Ca and P, were homogeneously distributed in every grains of NaClAp disk (Fig. 6b).

Microstructures and detailed microstructures of HAp disks (Fig. 7) and NaClAp disks (Fig. 8) after immersing in SBF for different time periods were examined by FE-SEM. No noticeable changes of microstructures were observed for HAp within 1 w. On the contrary, small acicular apatite crystals covered the whole NaClAp disk surface after only 3 h (Fig. 8a). Moreover, the thickness of newly formed apatite layer progressively increased with time.

Changes in the elemental concentrations of Ca, P, Na, and Cl as well as changes in pH and ionic activity product (IAP) of apatite upon soaking in SBF are shown in Fig. 9. No distinct changes were observed after immersing HAp in SBF. Specifically, immersing of HAp in SBF produced only a slight lessening in the concentrations of Ca and P while no change in the

Figure 2 FT-IR spectra of as-synthesized hydroxyapatite (HAp) and sodium and chloride co-substituted hydroxyapatite (NaClAp) powders.

Figure 4 XRD patterns obtained from hydroxyapatite (HAp) and sodium and chloride co-substituted hydroxyapatite (NaClAp) after sintering at 1100 °C for 3 h. Δ: hydroxyapatite and ●: chlorine-bearing hydroxyapatite.
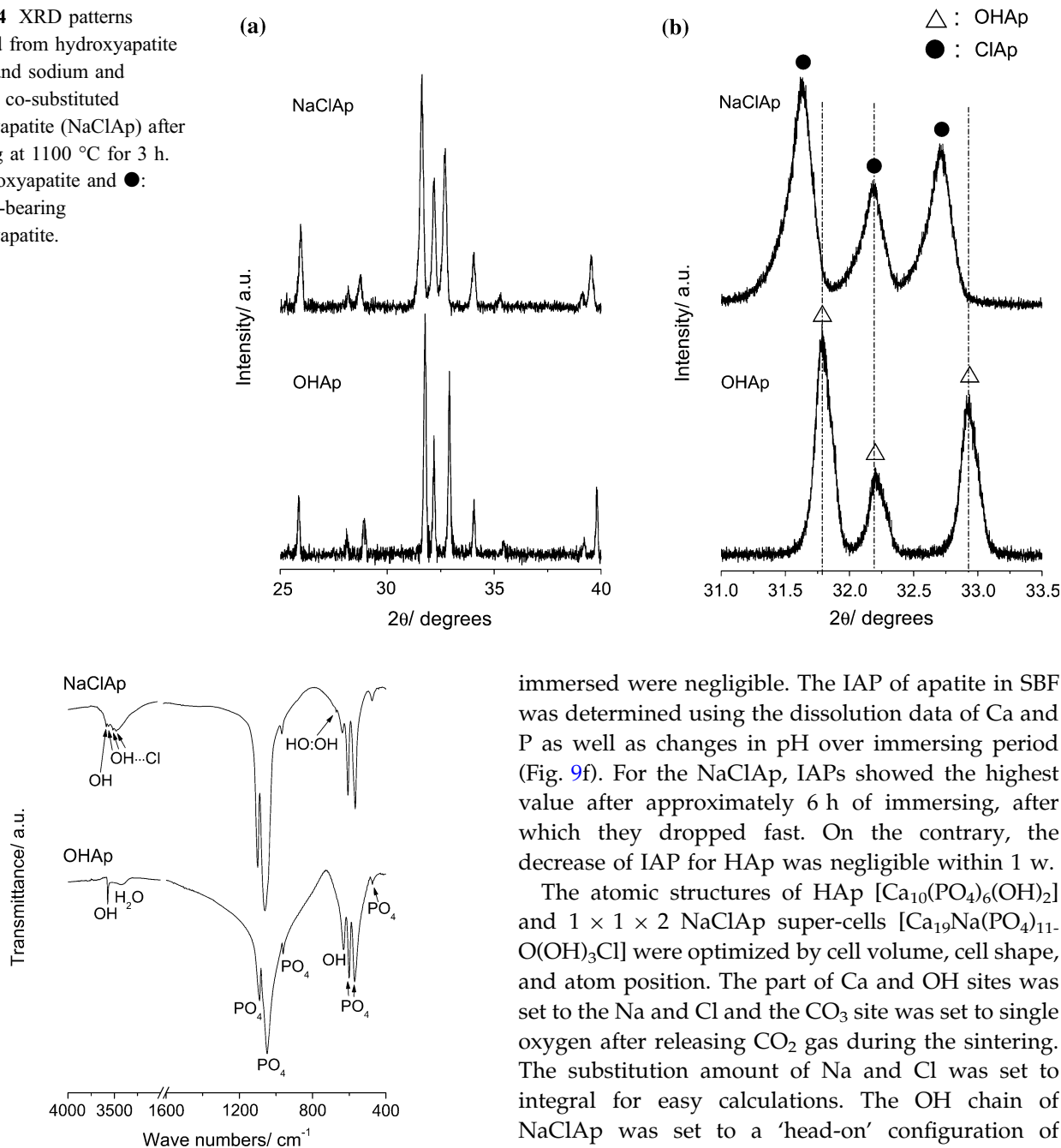

Figure 5 FT-IR spectra of hydroxyapatite (HAp) and sodium and chloride co-substituted hydroxyapatite (NaClAp) after sintering at 1100 °C for 3 h.

pH. On the contrary, the concentration of Ca and the pH of the SBF were increased up to 1 d by immersing NaClAp, but these measures decreased fast thereafter. Also, the concentration of P in the SBF a little dropped in the first 6 h and then decreased rapidly thereafter. Meanwhile, the changes of Na and Cl concentrations of the SBF in which NaClAp had been immersed were negligible. The IAP of apatite in SBF was determined using the dissolution data of Ca and P as well as changes in pH over immersing period (Fig. 9f). For the NaClAp, IAPs showed the highest value after approximately 6 h of immersing, after which they dropped fast. On the contrary, the decrease of IAP for HAp was negligible within 1 w.

The atomic structures of HAp [$Ca_{10}(PO_4)_6(OH)_2$] and $1 \times 1 \times 2$ NaClAp super-cells [$Ca_{19}Na(PO_4)_{11}O(OH)_3Cl$] were optimized by cell volume, cell shape, and atom position. The part of Ca and OH sites was set to the Na and Cl and the CO_3 site was set to single oxygen after releasing CO_2 gas during the sintering. The substitution amount of Na and Cl was set to integral for easy calculations. The OH chain of NaClAp was set to a 'head-on' configuration of HO:OH [36] along the [0 0 1] axis based on FT-IR result (Fig. 5). The atomic structures of the HAp unit cell (Fig. 10a) and $1 \times 1 \times 2$ Na and Cl co-substituted super-cells (Fig. 10b) in the crystal plane (1 0 0) with full ionic relaxation are shown in Fig. 10.

Table 1 shows the lattice constancies of apatites compared with experimental data (ab initio and Rietveld) and previous reports [37, 38]. The lattice constancies of HAp and NaClAp determined by PBE were in good agreement with results attained by the
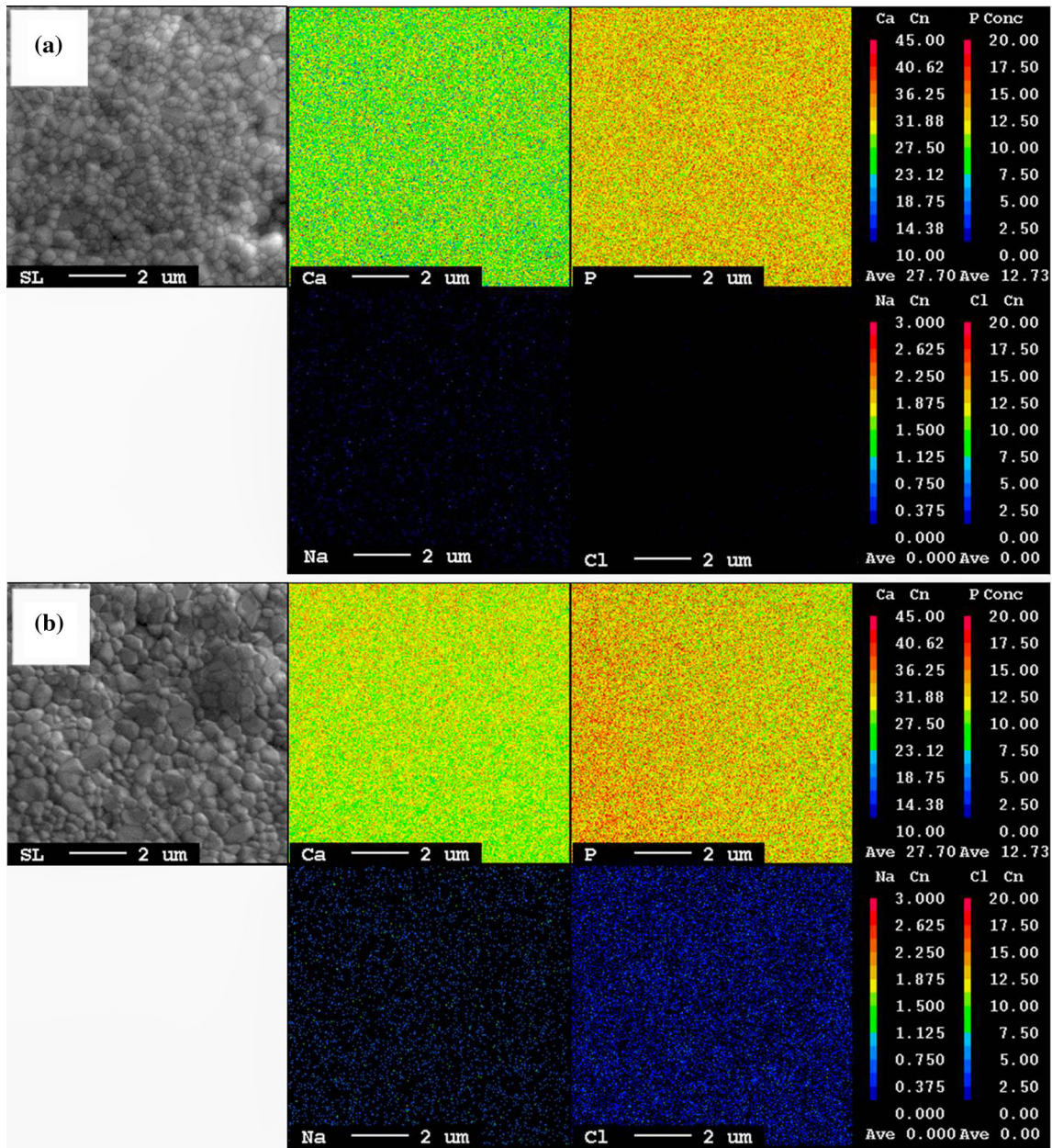
Figure 6 FE-SEM images and corresponding elemental maps measured by EPMA of calcium, phosphorous, sodium, and chlorine distributed in **a** hydroxyapatite (HAp) and **b** sodium and chloride co-substituted hydroxyapatite (NaClAp) disks after sintering at 1100 °C for 3 h.

Rietveld method and those reported earlier [37, 38] within approximately 1% error.

The total energy differences between HAp and NaClAp were determined with ΔE defined as:

$$\Delta E = E_{\text{tot}}(\text{NaClAp}) - 2 \times E_{\text{tot}}(\text{HAp}) + n\mu_{\text{Ca}} + n\mu_{\text{PO}_4} \\ + n\mu_{\text{OH}} + n\mu_{\text{H}} - n\mu_{\text{Na}} - n\mu_{\text{Cl}}$$

(1)

where $E_{\text{tot}}(\text{NaClAp})$ and $E_{\text{tot}}(\text{HAp})$ are the total energies of the corresponding systems; μ_{Ca}, μ_{PO_4}, μ_{OH}, μ_{H}, μ_{Na}, and μ_{Cl} are the chemical potentials of the corresponding systems; and n is the number of corresponding systems. The determined total energy difference between HAp and NaClAp was + 15.437 eV. This suggests that the structure of NaClAp was energetically more unstable than HAp.

Figure 7 FE-SEM images (5000×) of pure hydroxyapatite (HAp) disks after soaking in SBF for **a** 3 h, **b** 6 h, **c** 9 h, **d** 1 d, **e** 3 d, and **f** 7 d (inset micrographs show detailed microstructures, 20000×).
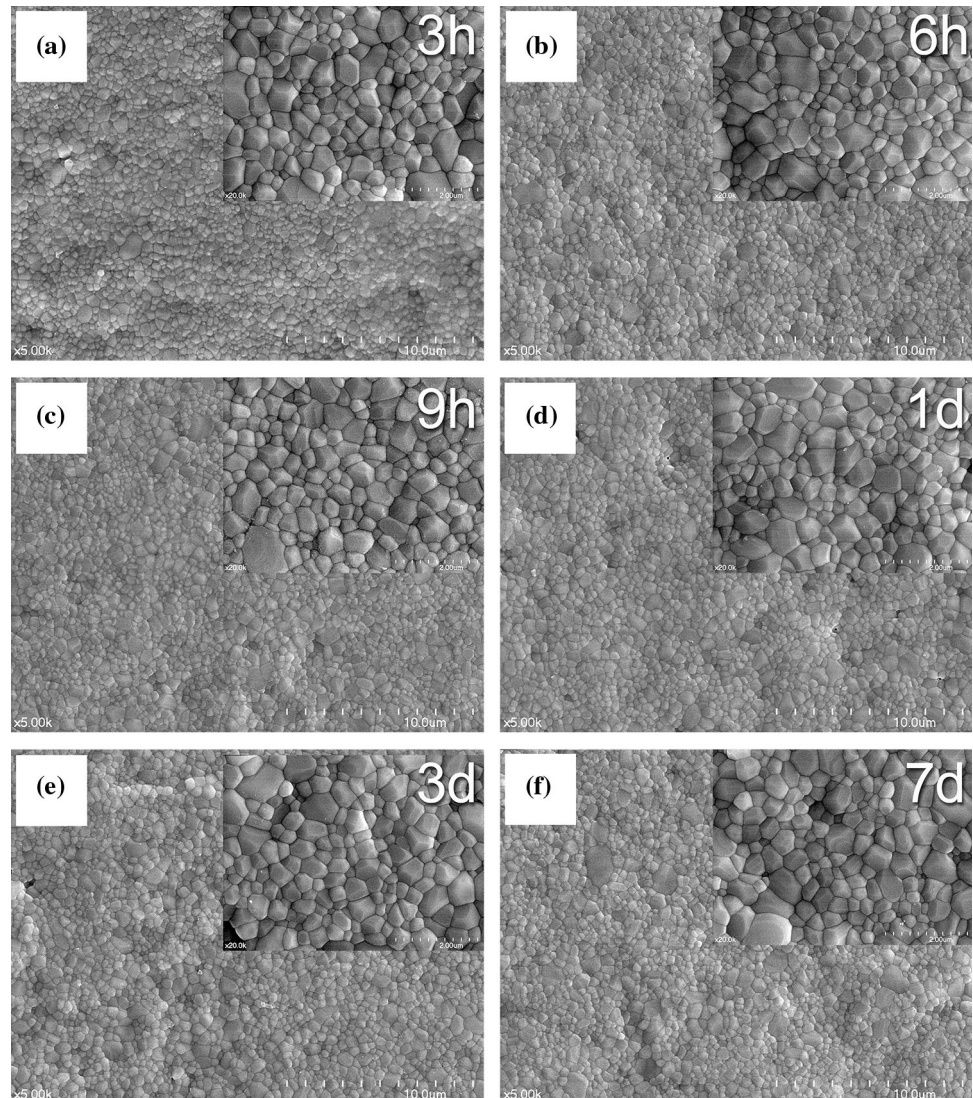

Table 2 shows the binding energies between apatite structures and the constituent elements of apatite. The binding energy was defined as

$$E_{bind} = E_{tot}(structure) - E_{tot}(structure - elements) + \mu_{elements}$$

(2)

where $E_{tot}(structure)$, $E_{tot}(structure - elements)$, and $\mu_{elements}$ are the total energies and chemical potentials of the corresponding systems, respectively. The differences of binding energies with the atomic positions in the crystal structures were negligible. Therefore, the average binding energies were used in this experiment (Table 2). The binding energies of Ca, PO$_4$, and OH were notably decreased by Na and Cl substitutions. This means that the bond between the NaClAp and its constituent elements came to be energetically unstable. The binding energies of Na and Cl were much smaller than other constituent elements. The higher total system energy and less stable binding energies of constituent elements of NaClAp compared to HAp explains the higher releasing behaviors of NaClAp in SBF (Fig. 9).

The osseointegration capacities of HAp and NaClAp granules were evaluated using a calvarial defect model in New Zealand white rabbits. Figure 11 displays the FE-SEM image of a NaClAp granule that was used for the osseointegration capacity test. The structure of the HAp granules was the same as that of NaClAp granules. Figure 12 displays the histological images of the calvarial defects after 4 w of surgery for each group. In case of HAp granules, they were mostly enclosed by connective tissues (pale blue) and the amount of newly formed

Figure 8 FE-SEM images (5000×) of sodium and chloride co-substituted hydroxyapatite disks (NaClAp) after soaking in SBF for **a** 3 h, **b** 6 h, **c** 9 h, **d** 1 d, **e** 3 d, and **f** 7 d (inset micrographs show detailed microstructures, 20000×).
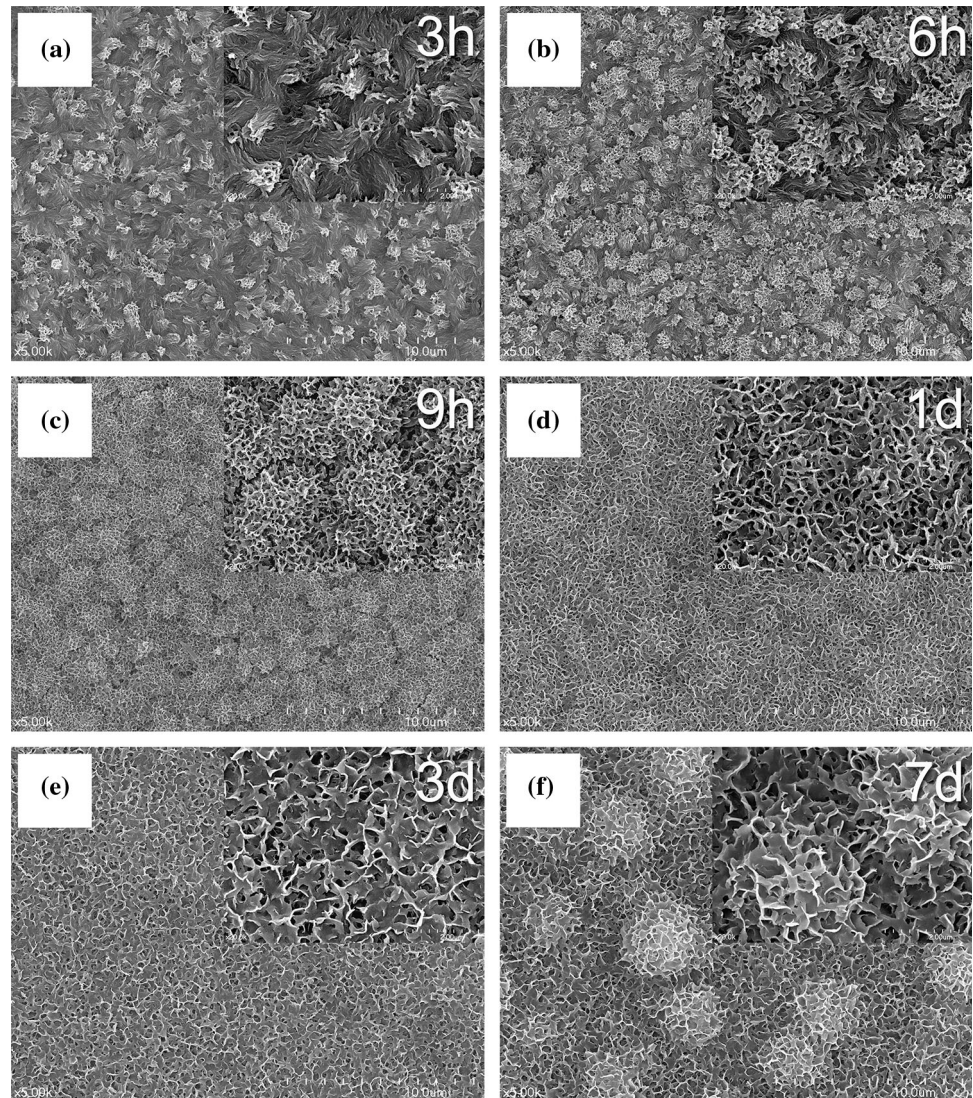
bone (pink) was small (Fig. 12a, c). On the contrary, the newly formed bone (pink) around the NaClAp granules (Fig. 12b, d) was dense and sound. The average occupied % of HAp granules was $48.3 \pm 4.5\%$, while that of NaClAp granules was $45.7 \pm 3.3\%$ ($p > 0.01$). The areal % of newly formed bone were $5.8 \pm 1.8\%$ for the HAp-treated defects while $52.4 \pm 6.1\%$ for NaClAp-treated defects ($p < 0.01$). Meanwhile, the areal % of soft tissue were $45.9 \pm 4.9\%$ for HAp-treated defects and $2.9\% \pm 1.5\%$ for NaClAp-treated defects, respectively ($p < 0.01$).

Discussion

In this study, the defect structures and their effects on the osseointegration capacity of sodium and chloride co-substituted hydroxyapatite were newly studied.

When $Ca(OH)_2$, H_3PO_4, $NaNO_3$, and NH_4Cl were reacted to produce NaClAp powder, Na-substituted low crystalline carbonate apatite powder with NH_4Cl was formed (Figs. 1, 2; Scheme 1). As the amount of Na substituting for Ca (x in Scheme 1) increased, CO_3 substitution for PO_4 was stoichiometrically scaled to balance the charge and mass.

The substitution of Na for Ca was confirmed by a little increased amount of CO_3 ions after preparation compared with the pure apatite counterpart (Fig. 2) [8]. Our evidence suggests that the substitution of Cl for OH did not occur at this stage: The chlorine-

Figure 9 Changes in concentrations of **a** calcium, **b** sodium, and **c** phosphorous as well as changes in **d** pH, **e** chlorine concentration, and **f** ionic activity products (IAP) of apatite in SBF after soaking hydroxyapatite (HAp) and sodium and chloride co-substituted hydroxyapatite (NaClAp) disks for the indicated time intervals.
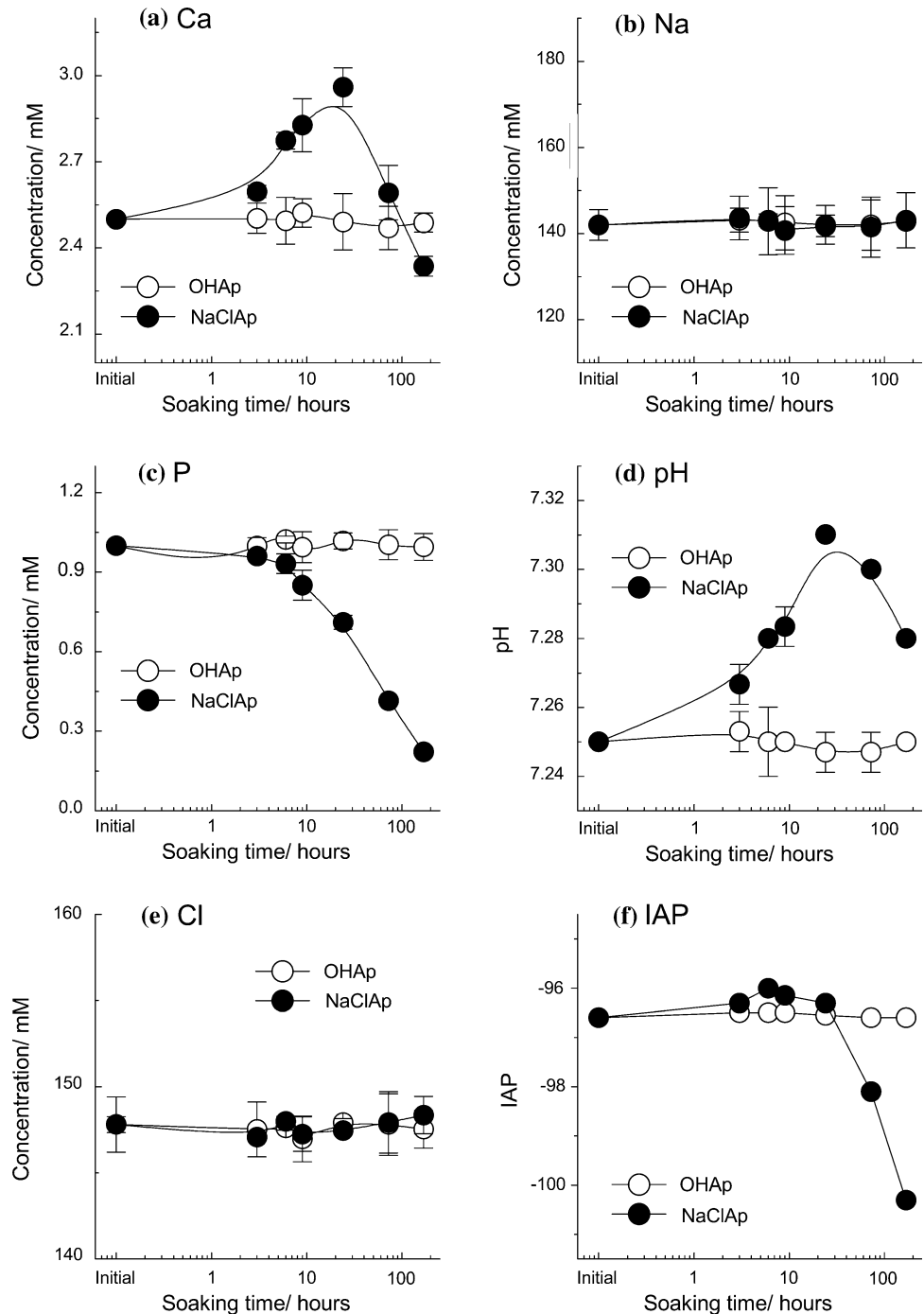
bearing apatite (ClAp) was not detected in XRD analysis (Fig. 1) and OH–Cl peaks, which occur at 3545, 3495, and 3460 cm^{-1} [35], were not observed in the FT-IR spectra (Fig. 2), either. Indeed, the substitution of Cl for OH has been reported to start above 600 °C [35] and this supports our results.

After sintering, Na and Cl co-substituted hydroxyapatite lacking carbonate ions (Scheme 2) was obtained.

The sintered NaClAp was the chlorine-bearing hydroxyapatite (Fig. 4) with a chlorine content of 0.59 according to JCPDS 70-0794 [39]. Similarly, the empirical formula of sintered NaClAp could be expressed as $Ca_{9.70}Na_{0.10}(PO_4)_{5.32}O_{0.68}(OH)_{1.51}Cl_{0.49}$
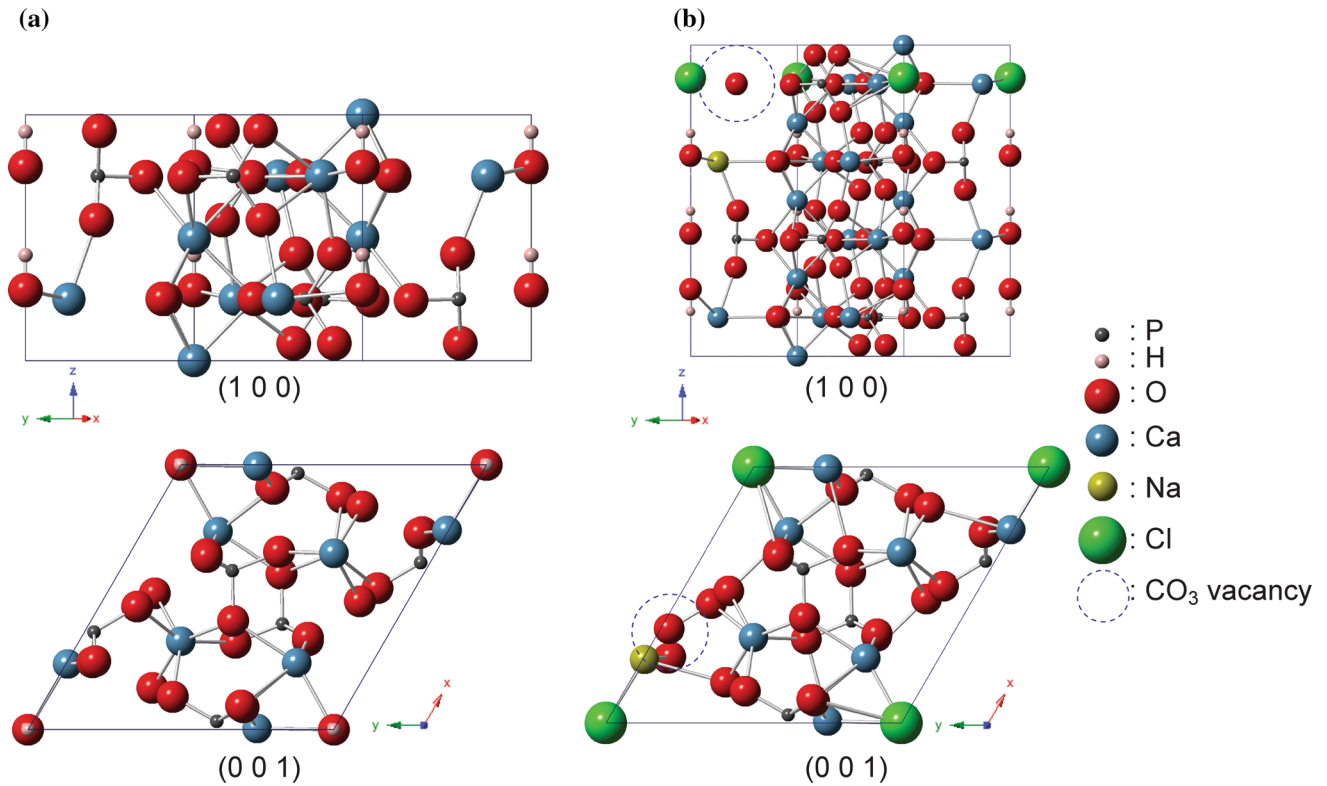
Figure 10 Crystal structures of **a** a hexagonal unit cell of hydroxyapatite (space group P6$_3$/m) consisting of 10 calcium atoms, 6 phosphorous atoms, 26 oxygen atoms, and 2 hydrogen atoms, **b** 1 × 1 × 2 super-cells of sodium and chloride co-substituted hydroxyapatite replacing one calcium ion with one sodium ion, one hydroxide ion with one chloride ion, and one oxygen ion at carbonate ion vacancy compared to the hydroxyapatite structure.

Table 1 Comparison of the lattice constancies a (Å) and c (Å) calculated by PBE and Rietveld methods with reported values [37, 38]

	a (Å)	c (Å)	c/a
OHAp (ab initio)	9.354	6.837	0.730
OHAp (*Rietveld*)	9.421	6.881	0.730
Ref. [37]	9.424	6.879	0.730
Ref. [38]	9.432	6.881	0.730
NaClAp (ab initio)	9.374	6.859	0.735
NaClAp (*Rietveld*)	9.354	6.849	0.732

Table 2 Comparison of the binding energies between the structures and constituent elements of the apatites

Structure	Atom	Binding energy (eV)
OHAp	Ca	− 12.01
	PO$_4$	− 17.06
	OH	− 6.35
NaClAp	Ca	− 7.58
	PO$_4$	− 16.59
	OH	− 6.04
	Na	− 4.07
	Cl	− 4.65

based on the reaction formula in Scheme 2. This means that about a quarter of the OH site was substituted with Cl. The large Cl ion prefers the halfway position between the Ca-triangles, whereas the OH ion places slightly above or below the plane of the three Ca [35]. With the increase in Cl concentration, the a-axis expands from 9.418 Å in the hydroxyapatite to 9.634 Å in the chlorapatite, while the c-axis contracts from 6.884 to 6.778 Å. This implies that the

unit cell volume expands with the Cl substitution [35] and explains the peak shift from the peak position of pure hydroxyapatite to chlorine-bearing hydroxyapatite (Fig. 4b). Meanwhile, the substituted amount of Na and Cl in NaClAp was less than those initially added and this is likely due to their volatilizations during the sintering process.
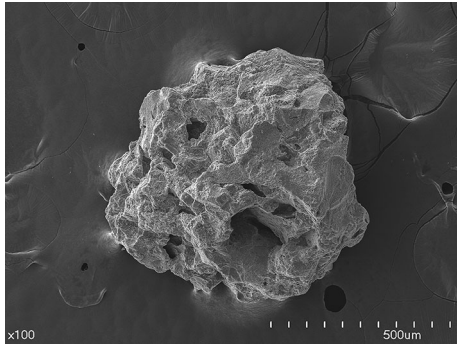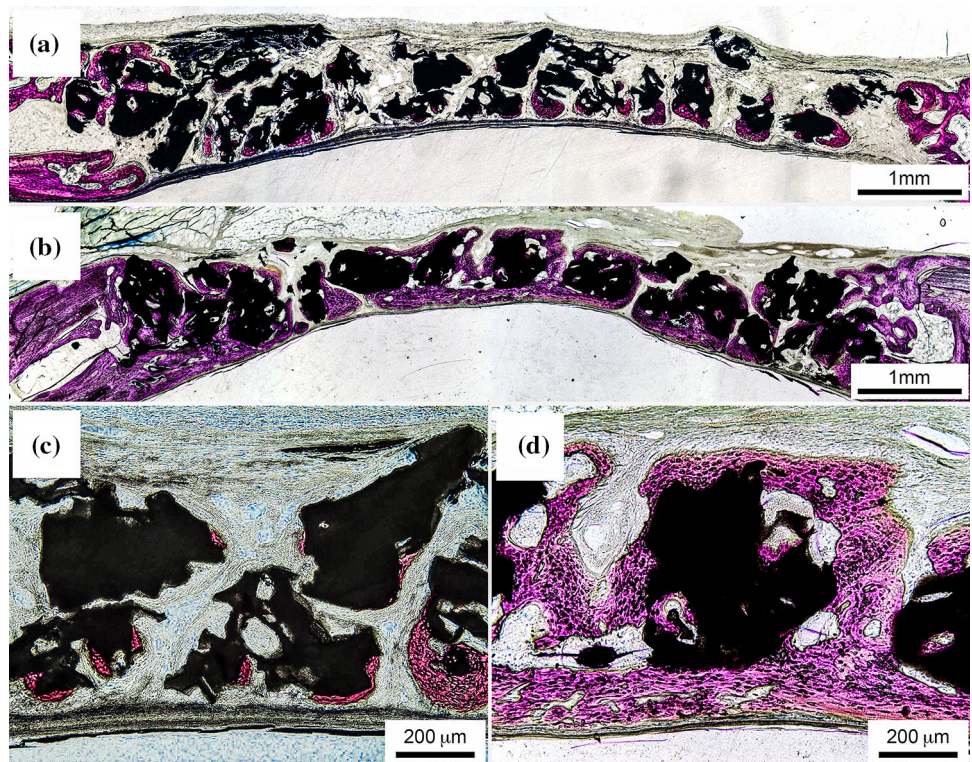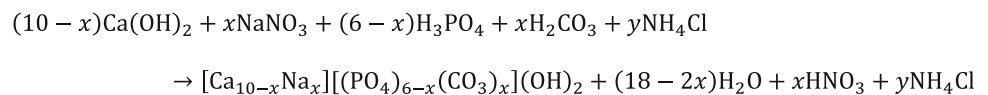
Figure 11 FE-SEM image of a sodium and chloride co-substituted hydroxyapatite (NaClAp) granule used for the osseointegration capacity test.
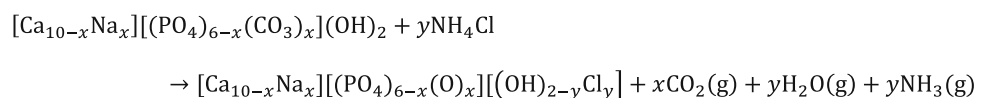
The substitution of Ca with Na produced negatively charged point defect (Na in the Ca site) as shown in Scheme 3. Meanwhile, the CO_3 ions in PO_4 site were thermally decomposed as CO_2 gas during sintering and produced positively charged point defect (O in the PO_4 site) as shown in Scheme 3. This phenomenon was described as the defect incorporation reaction following Kröger–Vink notation in Scheme 3 as balancing the charge and mass [20]. Concurrently, a portion of the OH sites also accommodated Cl (Schemes 2, 3), thereby generating OH–Cl bonds and caused a partially 'head-on' structure of HO:OH in an hydroxyl configuration (Fig. 5) [36].

Elemental mappings of HAp and NaClAp disks by EPMA (Fig. 6) supported XRD and FT-IR findings

Figure 12 Optical microscopic images of whole defects and more detailed images of porous hydroxyapatite [HAp, **a** original magnification × 40 and **c** original magnification × 100] and sodium and chloride co-substituted hydroxyapatite granules [NaClAp, **b** original magnification × 40 and **d** original magnification × 100] at 4 w after implantation into calvarial defects of New Zealand white rabbits. (Stained with Sanderson's Rapid Bone Stain^{TM} and a van Gieson counterstain).

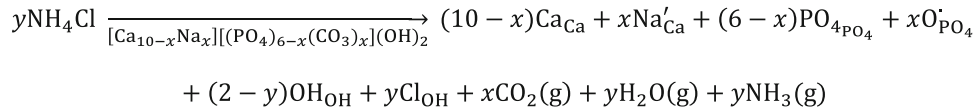**Scheme 1** Chemical reaction for reaction stage at room temperature.

$$(10 - x)Ca(OH)_2 + xNaNO_3 + (6 - x)H_3PO_4 + xH_2CO_3 + yNH_4Cl$$

$$\rightarrow [Ca_{10-x}Na_x][(PO_4)_{6-x}(CO_3)_x](OH)_2 + (18 - 2x)H_2O + xHNO_3 + yNH_4Cl$$

Scheme 2 Chemical reaction for sintering stage.

$$[Ca_{10-x}Na_x][(PO_4)_{6-x}(CO_3)_x](OH)_2 + yNH_4Cl$$

$$\rightarrow [Ca_{10-x}Na_x][(PO_4)_{6-x}(O)_x][(OH)_{2-y}Cl_y] + xCO_2(g) + yH_2O(g) + yNH_3(g)$$

$$yNH_4Cl \xrightarrow{[Ca_{10-x}Na_x][(PO_4)_{6-x}(CO_3)_x](OH)_2} (10-x)Ca_{Ca} + xNa'_{Ca} + (6-x)PO_{4_{PO_4}} + xO^{\cdot}_{PO_4}$$

$$+ (2-y)OH_{OH} + yCl_{OH} + xCO_2(g) + yH_2O(g) + yNH_3(g)$$

Scheme 3 Defect chemical reaction based on Kröger-Vink notation [20].

that Na and Cl were distributed homogeneously all over the apatite grain surfaces of the NaClAp disks (Fig. 6b) but not the HAp disks (Fig. 6a). Collectively, these results obviously implied the co-substitution of Na and Cl for the Ca and OH sites, respectively, of hydroxyapatite after sintering.

ICP-AES evaluation of SBF while NaClAp disks were soaking (Fig. 9) suggests a mechanism by which low crystalline hydroxyl carbonate apatite (HCA) formed on the surface of the NaClAp. The Ca (Fig. 9a) and OH ions (Fig. 9d) were continuously released from NaClAp disks up to 1 d. The subsequent decrease in the concentrations of Ca, P, and OH ions implied that consumption of these ions to form HCA crystals was faster than their release rate. It is noteworthy that the ionic activity product (IAP) of apatite in SBF showed a maximum value ($10^{-95.9}$) after approximately 6 h and decreased rapidly thereafter (Fig. 9f). Actually, the high maximum IAP coupled with the low solubility of apatite in water (5.5×10^{-118} at 37 °C [40]) was sufficient to produce nucleation and growth of apatite crystals in SBF. However, the changes in IAPs were also negligible for HAp disks (Fig. 9f). This observation supports only a minor producing capability of HCA on HAp (Fig. 7). Collectively, these results imply that the fast dissolution of Ca and OH ions from NaClAp into SBF resulted in apatite supersaturation and consequently induced the formation of HCA on the NaClAp disks.

The total system and binding energies of apatite can explain the dissolution behaviors of constituent elements of apatite in SBF. Specifically, the total system energy of NaClAp was markedly elevated compared with that of HAp (+ 15.437 eV) when Na was substituted for Ca and Cl for OH in HAp. Besides, the binding energies between apatite system and constituent elements of apatite (Ca, PO_4, and OH) decreased with Na and Cl co-substitution. This explains that the higher solubility of NaClAp compared with that of HAp in SBF.

The NaClAp, with enhanced HCA producing capability in SBF, demonstrated considerably higher osseointegration capacity compared with HAp

(Fig. 12). Specifically, dense and sound bone was formed on the NaClAp granules without intervening connective tissues. On the contrary, the amount of newly formed bone on HAp granules was small. These results are consistent with previous reports, which showed high capability to form HCA [41–48].

Together, the results of this study suggest that NaClAp has improved osseointegration capacity over HAp. The enhanced HCA producing capability in SBF and osseointegration capacity of NaClAp were largely attributed to improved solubility, which could be explained by a higher total system energy achieved by the formation of various defects. This means that the co-substitution of multiple ions into hydroxyapatite structure is a useful way to improve the osseointegration capacity of hydroxyapatite.

Conclusions

The defect structures of Na and Cl co-substituted hydroxyapatite and its osseointegration capacity were newly studied. Substitutions of Na for Ca and Cl for OH in HAp produced negatively charged sodium in calcium site, positively charged oxygen in phosphate site, OH–Cl bonds, and a partially 'head-on' structure of HO:OH in an hydroxyl configuration. These defects made NaClAp energetically unstable and consequently improved the HCA formation and osseointegration capacities. Taken together, our results indicate that the co-substitution of multiple ions into hydroxyapatite structure is a useful method to improve the osseointegration capacity of hydroxyapatite.

Acknowledgements

References

[1] Wopenka B, Pasteris JD (2005) A mineralogical perspective on the apatite in bone. Mater Sci Eng C 25:131–143. https://doi.org/10.1016/j.msec.2005.01.008

[2] Um S-H, Rhee S-H (2019) In vivo evaluations of hydroxyapatites with small and large grain sizes. Adv Appl Ceram 118:484–490. https://doi.org/10.1080/17436753.2019.1667176

[3] Pripatnanont P, Nuntanaranont T, Vongvatcharanon S, Limlertmongkol S (2007) Osteoconductive effects of 3 heat-treated hydroxyapatites in rabbit calvarial defects. J Oral Maxillofac Surg 65:2418–2424. https://doi.org/10.1016/j.joms.2007.06.619

[4] Takeshita F, Ayukawa Y, Iyama S, Suetsugu T, Oishi M (1997) Histological comparison of early wound healing following dense hydroxyapatite granule grafting and barrier placement in surgically-created bone defects neighboring implants. J Periodontol 68:924–932. https://doi.org/10.1902/jop.1997.68.10.924

[5] Carvalho AL, Faria PEP, Grisi MFM et al (2007) Effects of granule size on the osteoconductivity of bovine and synthetic hydroxyapatite: a histologic and histometric study in dogs. J Oral Implant 33:267–276. https://doi.org/10.1563/1548-1336(2007)33[267:EOGSOT]2.0.CO;2

[6] Kobayashi T, Nakamura S, Yamashita K (2001) Enhanced osteobonding by negative surface charges of electrically polarized hydroxyapatite. J Biomed Mater Res 57:477–484. https://doi.org/10.1002/1097-4636(20011215)57:4%3c477::AID-JBM1193%3e3.0.CO;2-5

[7] Fleckenstein KB, Cuenin MF, Peacock ME et al (2006) Effect of a hydroxyapatite tricalcium phosphate alloplast on

osseous repair in the rat calvarium. J Periodont 77:39–45. https://doi.org/10.1902/jop.2006.77.1.39

[8] Feki HE, Savariault JM, Salah AB (1999) Structure refinements by the Rietveld method of partially substituted hydroxyapatite: $Ca_9Na_{0.5}(PO_4)_{4.5}(CO_3)_{1.5}(OH)_2$. J Alloys Compd 287:114–120. https://doi.org/10.1016/S0925-8388(99)00070-5

[9] Gibson I, Best S, Bonfield W (1999) Chemical characterization of silicon-substituted hydroxyapatite. J Biomed Mater Res 44:422–428. https://doi.org/10.1002/(SICI)1097-4636(19990315)44:4%3c422::AID-JBM8%3e3.0.CO;2-%23

[10] El Feki H, Savariault JM, Salah AB, Jemal M (2000) Sodium and carbonate distribution in substituted calcium hydroxyapatite. Solid State Sci 2:577–586. https://doi.org/10.1016/S1293-2558(00)01059-1

[11] Landi E, Celotti G, Logroscino G, Tampieri A (2003) Carbonated hydroxyapatite as bone substitute. J Eur Ceram Soc 23:2931–2937. https://doi.org/10.1016/S0955-2219(03)00304-2

[12] Webster TJ, Massa-Schlueter EA, Smith JL, Slamovich EB (2004) Osteoblast response to hydroxyapatite doped with divalent and trivalent cations. Biomaterials 25:2111–2121. https://doi.org/10.1016/j.biomaterials.2003.09.001

[13] Wong CT, Chen QZ, Lu WW, Leong JCY, Chan WK, Cheung KMC, Luk KDK (2004) Ultrastructural study of mineralization of a strontium containing hydroxyapatite (Sr-HA) cement in vivo. J Biomed Mater Res 70A:428–435. https://doi.org/10.1002/jbm.a.30097

[14] Porter AE, Patel N, Brooks RA, Best SM, Rushton N, Bonfield W (2005) Effect of carbonate substitution on the ultrastructural characteristics of hydroxyapatite implants. J Mater Sci-Mater Med 16:899–907. https://doi.org/10.1007/s10856-005-4424-1

[15] Ni GX, Lu WW, Xu B et al (2006) Interfacial behaviour of strontium-containing hydroxyapatite cement with cancellous and cortical bone. Biomaterials 27:5127–5133. https://doi.org/10.1016/j.biomaterials.2006.05.030

[16] Landi E, Logroscino G, Proietti L, Tampieri A, Sandri M, Sprio S (2008) Biomimetic Mg-substituted hydroxyapatite: From synthesis to in vivo behaviour. J Mater Sci-Mater Med 19:239–247. https://doi.org/10.1007/s10856-006-0032-y

[17] Lima IR, Alves GG, Fernandes GVO, Dias EP, Soares GA, Granjeiro JM (2010) Evaluation of the in vivo biocompatibility of hydroxyapatite granules incorporated with zinc ions. Mater Res 13:563–568. https://doi.org/10.1590/S1516-14392010000400021

[18] Cho JS, Yoo DS, Chung YC, Rhee SH (2014) Enhanced bioactivity and osteoconductivity of hydroxyapatite through chloride substitution. J Biomed Mater Res 102A:455–469. https://doi.org/10.1002/jbm.a.34722

[19] Cho JS, Yoo DS, Chung YC, Lee JC, Rhee SH (2014) Enhanced osteoconductivity of sodium-substituted hydroxyapatite by system instability. J Biomed Mater Res Part B 102:1046–1062. https://doi.org/10.1002/jbm.b.33087

[20] Kröger FA, Vink HJ (1956) Relations between the concentrations of imperfections in crystalline solids. Solid State Phys 3:307–435. https://doi.org/10.1016/S0081-1947(08)60135-6

[21] Chappell H, Bristowe P (2007) Density functional calculations of the properties of silicon-substituted hydroxyapatite. J Mater Sci-Mater Med 18:829–837. https://doi.org/10.1007/s10856-006-0001-5

[22] Kokubo T, Kushitani H, Sakka S, Kitsugi T, Yamamuro T (1990) Solutions able to reproduce in vivo surface-structure changes in bioactive glass-ceramics A-W. J Biomed Mater Res 24A:721–734. https://doi.org/10.1002/jbm.820240607

[23] Kay MI, Young RA, Posner AS (1964) Crystal structure of hydroxyapatite. Nature 204:1050–1052. https://doi.org/10.1038/2041050a0

[24] Perdew JP, Chevary JA, Vosko SH, Jackson KA, Pederson MR, Filohais C (1992) Atoms, molecules, solids, and surfaces: applications of the generalized gradient approximation for exchange and correlation. Phys Rev B 46:6671–6687. https://doi.org/10.1103/PhysRevB.46.6671

[25] Vanderbilt D (1990) Soft self-consistent pseudopotentials in a generalized eigenvalue formalism. Phys Rev B 41:7892–7895. https://doi.org/10.1103/PhysRevB.41.7892

[26] Kresse G, Hafner J (1993) Ab initio molecular dynamics for liquid metals. Phys Rev B-Condens Matter 47:558–561. https://doi.org/10.1103/PhysRevB.47.558

[27] Hellmann H (1937) Einfuhrung in die quantumchemie. Deuicke, Leipzig

[28] Gillan MJ (1989) Calculation of the vacancy formation energy in aluminium. J Phys-Condens Matter 1:689. https://doi.org/10.1088/0953-8984/1/4/005

[29] Monkhorst HJ, Pack JD (1976) Special points for Brillouin-zone integrations. Phys Rev B 13:5188–5192. https://doi.org/10.1103/PhysRevB.13.5188

[30] Blöchl PE, Jepsen O, Andersen OK (1994) Improved tetrahedron method for Brillouin-zone integrations. Phys Rev B 49:16223–16233. https://doi.org/10.1103/PhysRevB.49.16223

[31] Nelson DGA, Featherstone JDB (1982) Preparation, analysis, and characterization of carbonated apatites. Calcif Tissue Int 34:S69-81. https://doi.org/10.1007/s00784-018-2453-7

[32] Arends J, Christoffersen J, Christoffersen MR et al (1987) A calcium hydroxyapatite precipitated from an aqueous solution: an international multimethod analysis. J Cryst Growth 84:512–532. https://doi.org/10.1016/0022-0248(87)90284-3

[33] Chickerur NS, Tung MS, Brown WE (1980) A mechanism for incorporation of carbonate into apatite. Calcif Tissue Int 32:55–62. https://doi.org/10.1007/BF02408521

[34] Silverstein RM, Bassler GC, Morril TC (1991) Spectrometric identification of organic compounds. Wiley, New York

[35] Maiti GC, Freund F (1981) Incorporation of chlorine into hydroxy-apatite. J Inorg Nucl Chem 43:2633–2637. https://doi.org/10.1016/0022-1902(81)80589-1

[36] Freund F, Knobel RM (1977) Distribution of fluorine in hydroxyapatite studied by infrared spectroscopy. J Chem Soc, Dalton Trans 1136–1140. https://doi.org/10.1039/DT9770001136

[37] Posner AS, Perloff A, Diorio AF (1958) Refinement of the hydroxyapatite structure. Acta Crystallogr 11:308–309. https://doi.org/10.1107/S0365110X58000815

[38] Sudarsanan K, Young RA (1969) Significant precision in crystal structural details. Holly Springs hydroxyapatite. Acta Crystallogr B 25:1534–1543. https://doi.org/10.1107/S0567740869004298

[39] Sudarsanan K, Young R (1978) Structural interactions of F, Cl and OH in apatites. Acta Crystallogr Sect B: Struct Crystallogr Cryst Chem 34:1401–1407

[40] McDowell H, Gregory TM, Brown WE (1977) Solubility of $Ca_5(PO_4)_3(OH)$ in the system $Ca(OH)_2$-H_3PO_4-H_2O at 5, 15, 25, and 37°C. J Res Natl Bur Stand 81A:273–281

[41] Ogino M, Ohuchi F, Hench LL (1980) Compositional dependence of the formation of calcium phosphate films on bioglass. J Biomed Mater Res 14:55–64. https://doi.org/10.1002/jbm.820140107

[42] Höland W, Vogel W, Naumann K (1985) Interface reaction between machinable bioactive glass–ceramics and bone. J Biomed Mater Res 19:303–312. https://doi.org/10.1002/jbm.820190311

[43] Anderson ÖH, Liu G, Karlsson KH, Miettinen J, Juhanoja J (1990) In vivo behavior of glasses in the SiO_2-Na_2O-CaO-P_2O_5-Al_2O_3-B_2O_3 system. J Mater Sci-Mater Med 1:219–227. https://doi.org/10.1007/BF00701080

[44] Ohtsuki C, Kushitani H, Kokubo T, Kotani S, Yamamuro T (1991) Apatite formation on the surface of ceravital-type glass-ceramic in the body. J Biomed Mater Res 25A:1363–1370. https://doi.org/10.1002/jbm.820251105

[45] Neo M, Kotani S, Nakamura T, Yamamuro T, Ohtsuki C, Kokubo T, Bando Y (1992) A comparative study of ultrastructures of the interfaces between four kinds of surface-active ceramic and bone. J Biomed Mater Res 26:1419–1432. https://doi.org/10.1002/jbm.820261103

[46] Kokubo T (2005) Design of bioactive bone substitutes based on biomineralization process. Mater Sci Eng C 25:97–104. https://doi.org/10.1016/j.msec.2005.01.002

[47] Kokubo T, Takadama H (2006) How useful is SBF in predicting in vivo bone bioactivity? Biomaterials 27:2907–2915. https://doi.org/10.1016/j.biomaterials.2006.01.017

[48] Kokubo T, Matsushita T, Takadama H, Kizuki T (2009) Development of bioactive materials based on surface chemistry. J Eur Ceram Soc 29:1267–1274. https://doi.org/10.1016/j.jeurceramsoc.2008.08.004